

Near-Field Wall-Modeled Large-Eddy Simulation of the NASA X-59 Low-Boom Flight Demonstrator

Emily Williams*, Gonzalo Arranz†, and Adrián Lozano-Durán‡
Massachusetts Institute of Technology, Cambridge, MA, 02142

Wall-modeled large-eddy simulation (WMLES) is utilized to analyze the experimental aircraft X-59 Quiet SuperSonic Technology (QueSST) developed by Lockheed Martin at Skunk Works for NASA’s Low-Boom Flight Demonstrator project. The simulations utilize the charLES solver and aim to assess the ability of WMLES to predict near-field noise levels under cruise conditions, considering various subgrid-scale (SGS) models and grid resolutions. The results are compared with previous numerical studies based on the Reynolds-averaged Navier-Stokes (RANS) equations. Our findings demonstrate that WMLES produces near-field pressure predictions that are similar to those of RANS simulations at a comparable computational cost. Some mild discrepancies are observed between the WMLES and RANS predictions downstream the aircraft. These differences persist for finest grid refinement considered, suggesting that they might be attributed to underresolved interactions of shock waves and expansions waves at the trailing edge.

Nomenclature

α_{ij}	=	resolved velocity gradient tensor
C_{dsm}	=	constant for dynamic Smagorinsky model
C_{vre}	=	constant for Vreman model
C_p	=	specific heat at constant pressure
C_v	=	specific heat at constant volume
δ_{ij}	=	Kronecker delta
γ	=	ratio of specific heats
h_{wm}	=	wall-normal matching location for the wall model
κ	=	Kármán constant
L_{BODY}	=	streamwise body-length of the X-59 model

*Department of Energy Computational Science Graduate Fellow, Department of Aeronautics and Astronautics, AIAA Student Member.

†Postdoctoral Associate, Department of Aeronautics and Astronautics, AIAA Member.

‡Boeing Assistant Professor, Department of Aeronautics and Astronautics, AIAA Senior Member.

M	=	Mach number
μ	=	dynamic viscosity
μ_M	=	Mach angle
$\mu_{t,wm}$	=	wall-model dynamic eddy viscosity
Pr	=	Prandtl number
Pr_t	=	turbulent Prandtl number
$Pr_{t,wm}$	=	turbulent Prandtl number for the wall model
p	=	pressure
p_∞	=	farfield pressure
p_s	=	pressure measured by the probe
q_j	=	heat flux vector
R	=	gas constant
Re	=	Reynolds number
ρ	=	density
ρ_∞	=	farfield density
S_{ij}	=	rate-of-strain tensor
σ_{ij}	=	shear-stress tensor
τ_{ij}	=	subgrid-scale tensor
$\tau_{w,wm}$	=	wall shear stress for the wall model
T	=	temperature
T_{wm}	=	wall-model temperature
u_i	=	velocity component
u_{wm}	=	magnitude of the wall-parallel velocity for the wall model
U_∞	=	farfield streamwise velocity
ε_p	=	relative difference in the pressure signature between the RANS and WMLES
x_i	=	spatial coordinate
X_N	=	transformed x -coordinate
y_n	=	wall-normal direction for wall model
ν	=	kinematic viscosity
ν_t	=	eddy viscosity
CFD	=	computational fluid dynamics
DLR	=	German Aerospace Center

EQWM	=	equilibrium wall-stress model
ECS	=	environmental control system
LES	=	large-eddy simulation
M	=	Mach number based on the freestream
SA	=	Spalart-Allmaras
RANS	=	Reynolds-averaged Navier–Stokes equations
SGS	=	subgrid scale
WMLES	=	wall-modeled large-eddy simulation

I. Introduction

The use of computational fluid dynamics (CFD) for external aerodynamic applications with increasing functionality and performance has greatly improved our understanding and predictive capabilities of complex flows [1]. However, applications to the modern aerospace industry often entail the presence of multi-scale, complex flow physics, which have since exposed limitations in even the most advanced CFD solvers [2]. One outstanding challenge in CFD is the prediction of quantities of interest in high-speed vehicles. In this work, we investigate the capability of wall-modeled large-eddy simulation (WMLES) to predict the near-field pressure signature of the X-59 Quiet SuperSonic Technology (QueSST).

The primary objective of NASA’s Low-Boom Flight Demonstrator project is to assess the viability of supersonic flight over land while minimizing noise levels. In this regard, the X-59 QueSST experimental aircraft, developed by Lockheed Martin at Skunk Works for NASA’s project, serves as a practical platform for validating high-speed aircraft CFD [3–5]. Previous research efforts, documented in the American Institute of Aeronautics and Astronautics (AIAA) Sonic Boom Prediction Workshop series, have encompassed near-field CFD models and subsequent atmospheric propagation to analyze noise signatures specific to the X-59 QueSST [6]. The workshop involved utilizing various CFD solvers to simulate near-field signatures, which were then propagated to the ground for noise level calculations. Currently, CFD studies of the X-59 QueSST mostly rely on closure models for the Reynolds-averaged Navier-Stokes (RANS) equations [7, 8], along with other variations [9, 10]. Here, we use as a reference the near-field RANS simulations from Kirz [11]. The RANS cases were performed with the German Aerospace Center (DLR) TAU code, which is based on an unstructured finite-volume approach for solving the RANS equations on hybrid grids [11, 12]. An improved second-order accurate advection upstream splitting method (AUSM) upwind scheme was applied for the spatial discretization of the convective fluxes, and an implicit lower upper symmetric Gauss Seidel scheme is used for time stepping. The AUSM scheme is a flux splitting scheme with an aim at removing numerical dissipation on a contact discontinuity for accurate and robust resolution for shocks [13]. The gradients were computed using a Green Gauss

approach. The Spalart-Allmaras (SA)-negative turbulence model was used. For a comprehensive overview of the RANS simulations, refer to the work by Park and Carter [6].

Current RANS methodologies have demonstrated high performance in predicting shock waves far from their interactions with boundary layers [8]. Yet, there is still no practical RANS model that can accurately address the wide range of flow regimes relevant to aerodynamic vehicles. These regimes include separated flows, afterbodies, mean-flow three-dimensionality, shock waves, aerodynamic noise, fine-scale mixing, laminar-to-turbulent transition, and more. RANS predictions in these scenarios often lack consistency and reliability, particularly when dealing with geometries and conditions representative of the flight envelope of airplanes [2]. One notable example is the inadequate prediction of the onset and extent of three-dimensional separated flow in wing-fuselage junctures, where RANS-based approaches have exhibited poor performance [14, 15]. Furthermore, CFD experiments with aircraft at high angles of attack have revealed that RANS-based solvers struggle to accurately predict maximum lift, the corresponding angle of attack, and the physical mechanisms underlying stall. While algebraic RANS closures, such as the Baldwin–Lomax model [16], offer reasonable predictions at high Mach number boundary layer flows [17], they are still deficient in capturing separated flows [18].

Recently, large-eddy simulation (LES) has gained momentum as a tool for aerospace applications that might offer a higher degree of generality compared to RANS approaches [19]. In LES, the large eddies containing most of the energy are directly resolved, while the dissipative effect of the small scales is modeled through a subgrid-scale (SGS) model. By incorporating a near-wall flow model that resolves only the large-scale motions in the outer region of the boundary layer, WMLES reduces the grid-point requirements, scaling at most linearly with increasing Reynolds number [20, 21]. Some representative studies of WMLES at high-speed conditions include shock/boundary-layer interactions [22–24], compressible channels [25, 26], the shock wave boundary layer interaction over compression ramps [27, 28], flow past a single fin [29], flow past two parallel fins [30], turbulent boundary layers [31, 32] and turbulent channel flows [33], transitional flows [34], the wall-mounted hump and axisymmetric compression ramp [35, 36], and transonic airfoils [37]. Although most SGS/wall models are rooted in aero/thermal equilibrium assumptions, which are only valid for incompressible flows, the general consensus is that WMLES is able to capture key flow physics. Nonetheless, the use of WMLES for the prediction of realistic supersonic aircraft has been explored to a lesser extent, which is the goal of this work.

Our long-term objective is to develop a SGS model for WMLES that provides accurate predictions across a wide range of flow regimes, including subsonic and supersonic flows [38–41]. The results from the present study will inform the advances required to extend our SGS modeling approach in the presence of shock waves.

This paper is organized as follows. The methodology of WMLES is presented in section II, which contains details of the numerical solver, and the physical and computational setups are discussed in section III. The numerical results for the quantities of interest are presented in section IV. Finally, conclusions and future work are offered in section V.

II. Methodology

A. SGS Models

The performance of WMLES is investigated for two SGS models. Both models adopt the eddy viscosity form

$$\tau_{ij} = -2\nu_t \left(\widetilde{S}_{ij} - \frac{1}{3} \widetilde{S}_{kk} \delta_{ij} \right) + \frac{1}{3} \tau_{kk} \delta_{ij}, \quad (1)$$

where repeated indices imply summation, τ_{ij} the SGS tensor, ν_t is the eddy viscosity, S_{ij} is the rate-of-strain, $\tau_{kk} \delta_{ij} / 3$ is the isotropic component of the SGS tensor with Kronecker delta δ_{ij} , and $\widetilde{\phi} = \overline{\rho \phi} / \overline{\rho}$ is the Favre average with $\overline{(\cdot)}$ denoting the grid filter.

The first SGS model considered is the dynamic Smagorinsky model (labeled as DSM) [42], where the eddy viscosity is given by $\nu_t = C_{\text{dsm}} |\widetilde{S}|$. The constant C_{dsm} is dynamically computed as [43]

$$C_{\text{dsm}} = \frac{1}{2} \frac{\langle \mathcal{L}_{ij} \mathcal{M}_{ij} \rangle}{\langle \mathcal{M}_{ij}^2 \rangle} \quad (2)$$

where

$$\mathcal{L}_{ij} = \overline{\rho} \left(\widetilde{\widehat{u}_i \widehat{u}_j} - \widehat{u}_i \widehat{u}_j \right), \quad \mathcal{M}_{ij} = \left(\widehat{\Delta} / \Delta \right)^2 |\widetilde{S}| \left(\widetilde{S}_{ij} - \frac{1}{3} \widetilde{S}_{kk} \right) - |\widetilde{S}| \left(\widetilde{S}_{ij} - \frac{1}{3} \widetilde{S}_{kk} \right),$$

with $\widehat{(\cdot)}$ being the test filter with filter width $\widehat{\Delta}$ larger than that of the grid filter Δ , and $|\widetilde{S}|^2 = 2 \widetilde{S}_{ij} \widetilde{S}_{ij}$.

The second SGS model considered is the Vreman model [44] (labeled as Vreman). The eddy viscosity is given by

$$\nu_t = C_{\text{vre}} \sqrt{\frac{B_\beta}{\alpha_{ij} \alpha_{ij}}}, \quad (3)$$

where $\alpha_{ij} = \partial \overline{u}_j / \partial x_i$, $\beta_{ij} = \Delta^2 \alpha_{mi} \alpha_{mj}$, and $B_\beta = \beta_{11} \beta_{22} - \beta_{12}^2 + \beta_{11} \beta_{33} - \beta_{13}^2 + \beta_{22} \beta_{33} - \beta_{23}^2$. The model constant $C_{\text{vre}} \approx 0.07$.

For both the Vreman model and the DSM, the term $\tau_{kk} \delta_{ij}$ is neglected on the grounds that it is small compared to the thermodynamic pressure. The SGS model for the heat flux in the energy equation is given by the eddy diffusivity model $q_i = -\overline{\rho} \nu_t / \text{Pr}_t \partial \widetilde{T} / \partial x_i$, where T is the temperature, and Pr_t is the turbulent Prandtl number which is set equal to 0.9. The equation of state for the fluid is a calorically perfect gas $\overline{p} = \overline{\rho} R \widetilde{T}$. Additional details about the computational approach can be found in Fu et al. [45].

B. Wall Model

We use a compressible equilibrium wall-stress model (EQWM) to model the small-scale flow motions near the wall. Figure 1 shows a schematic of the wall modeling approach. The form of the wall model is given by two ordinary

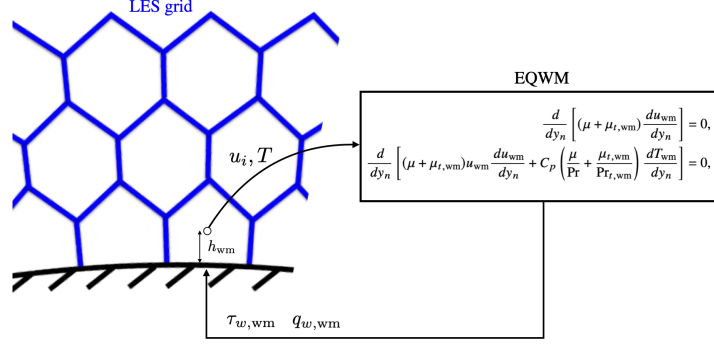


Fig. 1 Schematic of the equilibrium wall model.

differential equations derived from the conservation of momentum and energy by neglecting the wall-parallel fluxes [46],

$$\frac{d}{dy_n} \left[(\mu + \mu_{t,wm}) \frac{du_{wm}}{dy_n} \right] = 0, \quad (4a)$$

$$\frac{d}{dy_n} \left[(\mu + \mu_{t,wm}) u_{wm} \frac{du_{wm}}{dy_n} + C_p \left(\frac{\mu}{Pr} + \frac{\mu_{t,wm}}{Pr_{t,wm}} \right) \frac{dT_{wm}}{dy_n} \right] = 0, \quad (4b)$$

where y_n is the wall-normal direction, u_{wm} is the magnitude of the wall-parallel velocity for the wall model, T_{wm} is the wall-model temperature, μ is the dynamic viscosity, $\mu_{t,wm}$ is the wall-model eddy viscosity, Pr and $Pr_{t,wm}$ are Prandtl number and turbulent Prandtl number, respectively, and C_p is the specific heat at constant pressure. The eddy viscosity is taken from the mixing-length model as

$$\mu_{t,wm} = \kappa \bar{\rho} y_n \sqrt{\frac{\tau_{w,wm}}{\bar{\rho}}} \left[1 - \exp\left(\frac{-y_n^+}{A^+}\right) \right]^2, \quad (5)$$

where $\kappa = 0.41$, $Pr_{t,wm} = 0.9$, $A^+ = 17$, $\bar{\rho}$ is the density, $\tau_{w,wm}$ is the instantaneous wall shear stress, and superscript $+$ denotes quantities normalized by τ_w and μ . At $y_n = 0$, Eq. (4) is complemented with the non-slip and adiabatic wall boundary conditions. At $y_n = h_{wm}$, u_{wm} and T_{wm} are set equal to the instantaneous values from the LES solution. The matching location h_{wm} is taken at the centroid of the first control volume attached to the wall. Effectively, given an instantaneous wall-parallel velocity and temperature at some height above the wall, Eq. 4 is solved for u_{wm} and T_{wm} in an overlapping layer between $y_n = 0$ and $y_n = h_{wm}$. The solution from the wall shear stress ($\tau_{w,wm}$) and the wall heat flux ($q_{w,wm}$) from the wall model are returned to the LES solver as boundary conditions at the wall.

C. Numerical Solver and Computational Resources

The simulations are performed using the CPU version of the code charLES from Cascade Technologies (Cadence). The validation of the algorithm can be found in Fu et al. [30]. The solver integrates the filtered Navier-Stokes equations



Fig. 2 The C608 configuration of the X-59 from Park and Carter [6].

using a second-order accurate finite volume formulation. The numerical discretization relies on a flux formulation that is approximately entropy preserving in the inviscid limit, thereby limiting the amount of numerical dissipation added into the calculation. No special treatment was employed for the shock waves, and the simulations in the present work are conducted without a shock capturing scheme or sensor. The time integration is performed with a third-order Runge-Kutta explicit method. The mesh generator is based on a Voronoi hexagonal close packed point-seeding method which automatically builds high-quality meshes for arbitrarily complex geometries with minimal user input.

All simulations in this work are performed using high-performance computing (HPC) resources provided by the MIT Supercloud. The MIT Supercloud is a collaboration with MIT Lincoln Laboratory on a shared facility that is optimized for streamlining open research [47]. The system is designed to support work that requires significant compute or memory resources. The system has 480 nodes with Intel Xeon Platinum 8260 processors with 2×24 CPUs/node and 192GB of RAM per node.

III. Computational Setup

The simulation is performed using the C608 Low-Boom Flight Demonstrator geometry provided by the AIAA Sonic Boom Prediction workshop shown in Figure 2. This geometry configuration is an early iteration of the X-59 final design and is desirable for comparing against RANS results using the same setup. Simulations are performed at cruise conditions at Mach number $M = 1.4$ and Reynolds number per inch of $Re/in = 109,776$. Freestream and boundary conditions are specified in Table 1. The C608 has propulsion and environmental control system (ECS) boundary conditions as shown in Figure 3. The engine bypass exhaust is a semicircular region between the nozzle and aft deck, and the ECS inlet is located in the wing root [6].

The size of the computational domain is $2.7L_{BODY} \times 2.7L_{BODY} \times 5.4L_{BODY}$ in the streamwise, spanwise, and vertical directions, respectively, where L_{BODY} is the streamwise body-length of the model. Figure 4 shows a schematic of the computational domain, where the red line denotes the pressure probe placed at one-body length below directly

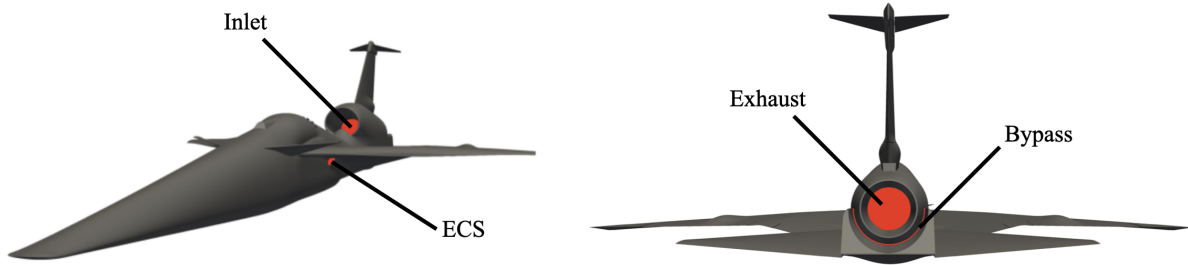


Fig. 3 C608 boundary conditions.

Table 1 C608 freestream and boundary conditions

Description	Condition
Freestream Mach number	1.4
Freestream temperature (°R)	389.9
Altitude (ft)	53,200
Unit Reynolds number (per inch)	109,776
Ratio of engine nozzle plenum total pressure to freestream static pressure	10.0
Ratio of engine nozzle plenum total temperature to freestream static temperature	7.0
Ratio of engine bypass exhaust total pressure to freestream static pressure	2.4
Ratio of engine bypass exhaust total temperature to freestream static temperature	2.0
Ratio of engine fan face static pressure to freestream	2.6
Ratio of ECS inlet static pressure to freestream	1.4

Table 2 Summary of grid resolution and SGS model for X-59 flow cases conducted with WMLES

Case	Mach-aligned cone		Probe-containing plane		SGS model
	in/cell	Points/ L_{BODY}	in/cell	Points/ L_{BODY}	
1	20	54	10	108	DSM
2	10	108	5	216	DSM
3	5	216	2.5	432	DSM
4	20	54	10	108	Vreman
5	10	108	5	216	Vreman
6	5	216	2.5	432	Vreman

under the aircraft.

A total of six WMLES cases are conducted for three different grid resolutions using both DSM and Vreman models. In all cases, the domain is discretized using a Mach-aligned cone of length $2.1L_{BODY}$ and whose vertex is located at $0.1L_{BODY}$ upstream the aircraft nose, and an additional grid refinement in the probe-containing plane where the pressure signatures are reported. This additional refined region extends from the aircraft nose to $2.2L_{BODY}$ in the streamwise direction, to $0.25L_{BODY}$ in the spanwise direction (enclosing the wing of the aircraft), and to $1.5L_{BODY}$ below the aircraft. The cases also include enhanced refinement around the body of the aircraft geometry. Table 2 compiles the information for the six cases, including the grid size in the Mach-aligned cone and the probe-containing refined plane. As an example, Figure 5a shows the domain discretization for one of the WMLES cases in a slice of the x - z plane. Figure 5b shows a view of the domain from the front of the aircraft at a slice halfway through the domain. The front and side views show the refinement configuration with a red line to denote the pressure probe. Figure 5c shows a top view of the domain discretization.

IV. Results

A. Shock Waves

First, we discuss the results for the locations and intensities of shock waves observed from both the side and top views, depicted in Figure 6a and Figure 7a, respectively. We label the shocks that arise due to the aircraft’s geometry and the boundary conditions. Additionally, we provide computational flow visualizations of the side and top views in Figure 6b and Figure 7b, respectively. These visualizations are generated to capture the contours in the relative pressure, denoted as p , which is defined as the percent difference deviation from the freestream pressure

$$p = \frac{\Delta p}{p_\infty} \times 100, \quad (6)$$

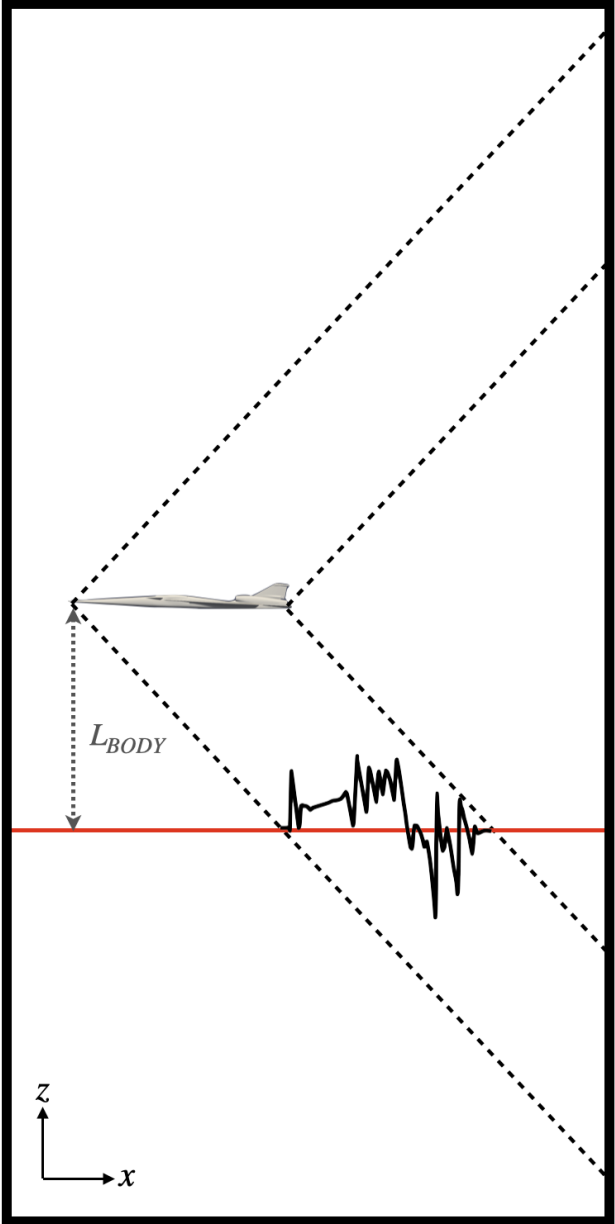
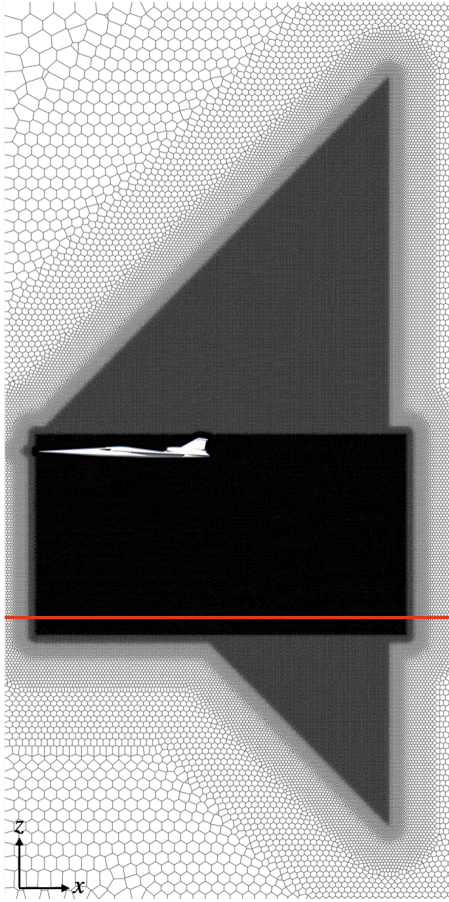
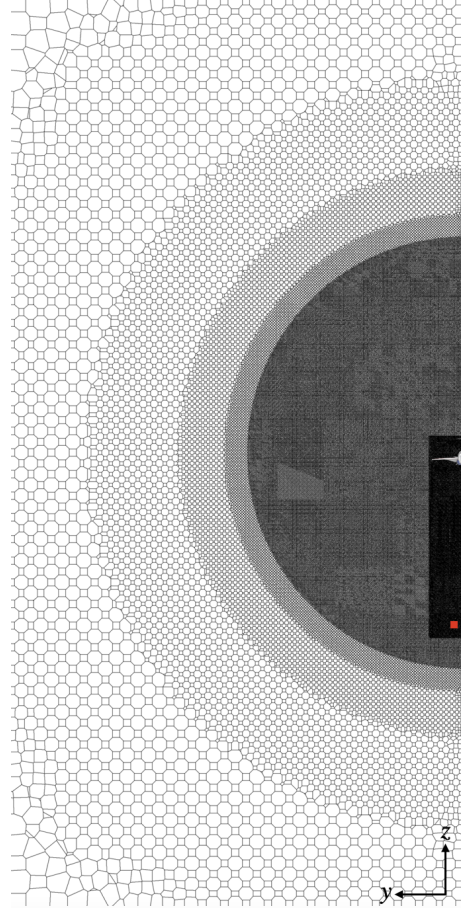


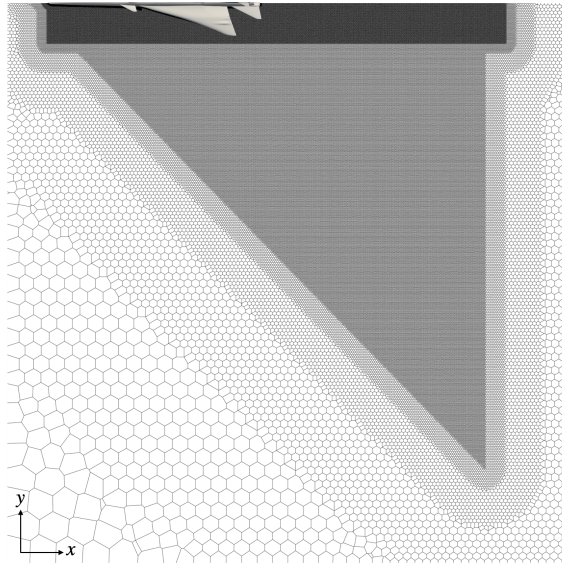
Fig. 4 Computational domain for X-59 simulations.



(a) Side view of the WMLES grid topology across the x - z plane. The red line indicates the location of the pressure probe.



(b) Front view of the WMLES grid topology across the y - z plane. The red line indicates the location of the pressure probe.



(c) Top view of the WMLES grid topology across the x - y plane.

Fig. 5 Grid topology for cases 3 and 6.

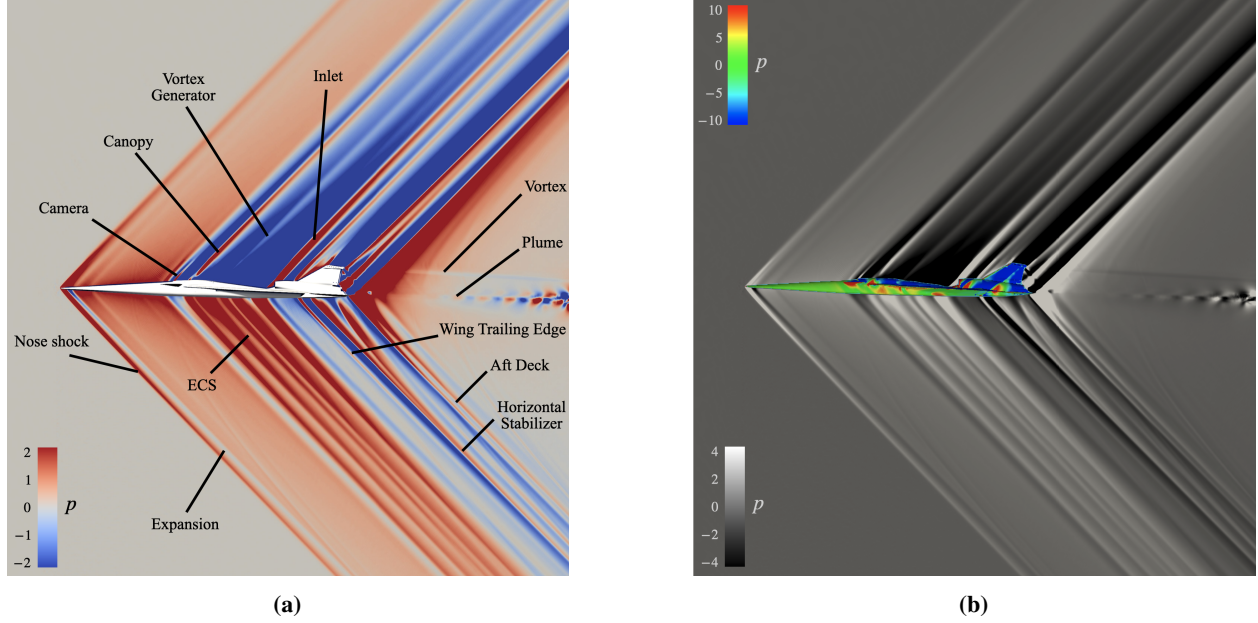


Fig. 6 Pressure visualizations for case 3. (a) Pressure contours in the $y/L_{BODY} = 0$ plane and (b) side view of the pressure distribution over the aircraft.

where $\Delta p = p_s - p_\infty$ where p_s is the pressure measured by the probe and

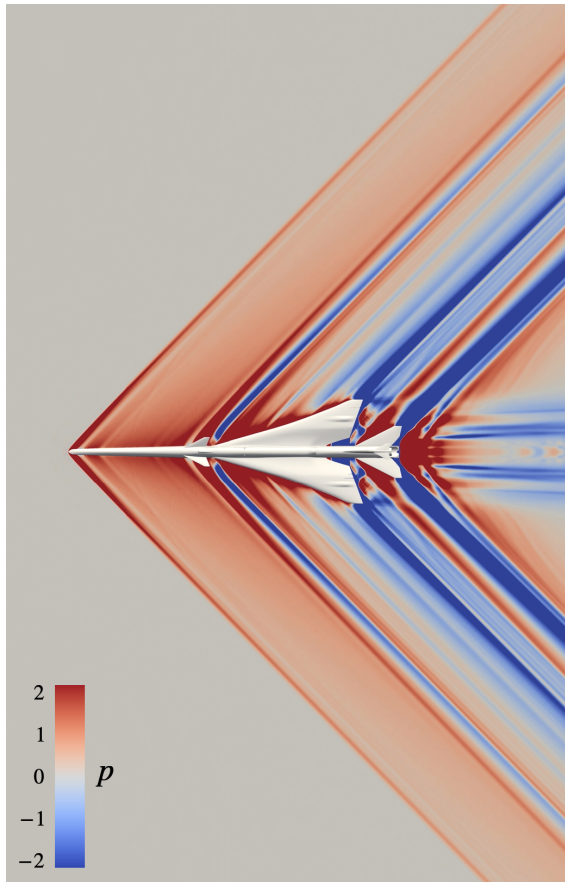
$$p_\infty = \frac{\rho_\infty}{\gamma} \left(\frac{U_\infty}{M} \right)^2. \quad (7)$$

where the subscript ∞ denotes freestream quantity, $\gamma = 1.4$, and $M = 1.4$. The pressure visualizations show the surface pressure distribution on the aircraft, also quantified using p above. The nose creates a shock and expansion pair, followed by a smooth compression. There is a rapid succession of shocks and expansions generated by the wing leading edge, vortex generators, and ECS inlet. The wing trailing edge, horizontal stabilizer, aft deck, tail, plume, and vortices result in additional shocks and expansions along with other complex interactions. The surface pressure distribution indicates that the inlet spillage creates an area of high pressure over the wing. These results are consistent with those reported through the AIAA Sonic Boom Prediction Workshop [6].

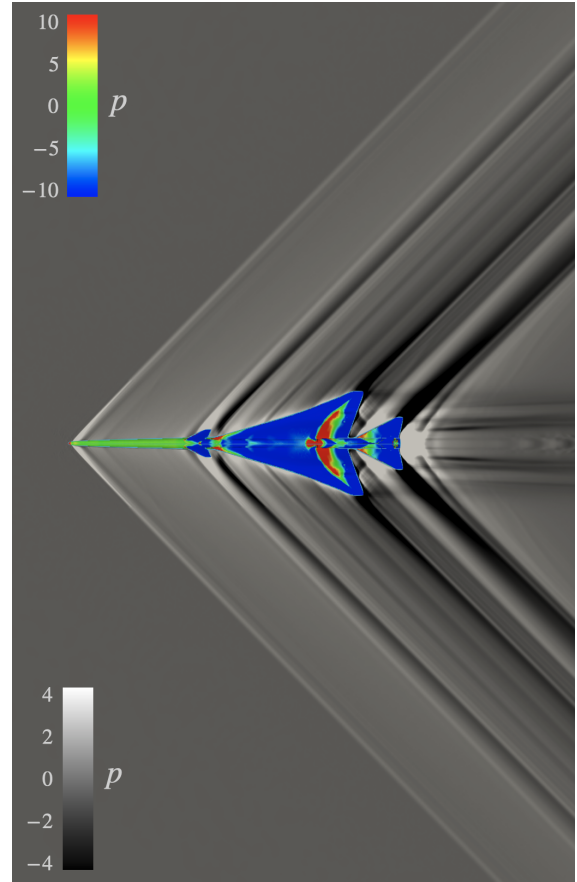
B. Pressure Signatures

The WMLES pressure signatures at one-body length away from the aircraft are compared with RANS results from Kirz [11] for a grid resolution of 5.74 in/cell. We define a transformed x-coordinate given by

$$X_N = x - \frac{L_{BODY}}{\tan(\mu_M)}, \quad (8)$$

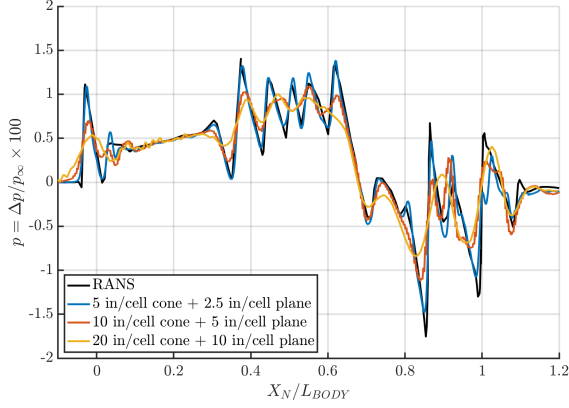


(a)

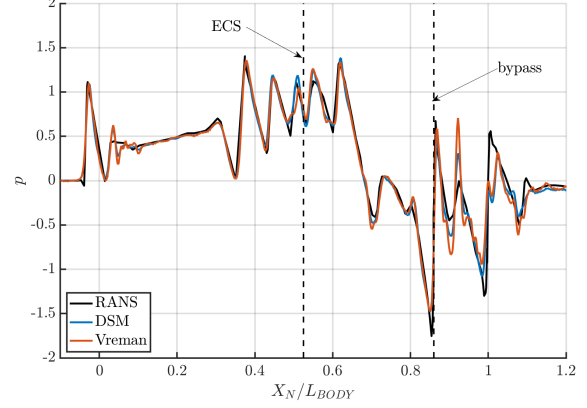


(b)

Fig. 7 Pressure visualizations for case 3 (cont.). (a) Pressure contours in the $z/L_{BODY} = 0$ plane and (b) top view of the pressure distribution over the aircraft.



(a) Pressure signature for DSM and different resolutions (cases 1-3) as a function of X_N/L_{BODY} .



(b) Pressure signature for DSM and Vreman for the finest grid resolution considered (cases 3 and 6) as a function of X_N/L_{BODY} .

Fig. 8 Near-field pressure signatures.

where the distance from the nose in the freestream direction x is normalized by the Mach angle $\mu_M = \sin^{-1}(1/M)$ using the radial distance to the model, L_{BODY} in this case. This transformation is common in previous sonic boom simulations [11].

Figure 8a shows the prediction of the pressure signature by WMLES with the DSM for the different grid refinement configurations outlined in Table 2. As the grid is refined, the prediction provided by WMLES approaches the RANS results for the near-field pressure signature. Results computed using the Vreman SGS model were comparable and are omitted for the sake of brevity. Figure 8b shows the finest resolution case comparison with both SGS models.

The WMLES solutions show reasonably accurate agreement with the RANS results for $X_N/L_{BODY} < 0.9$ for both SGS models, particularly at the finest grid resolution. This is also the case in the vicinity of the ECS and bypass, located approximately at $X_N/L_{BODY} \approx 0.45$ and $X_N/L_{BODY} \approx 0.85$, respectively. However, we observe that WMLES results do not match the RANS solution as effectively in the downstream region and after the aircraft. This disparity is present for both SGS models and persists for the finest grid resolution considered. Although the specific cause of this disparity remains unclear, it is likely attributed to the intricate interactions and rapid sequence of shocks and expansions occurring near various components, including the wing trailing edge, horizontal stabilator, aft deck, T-tail, engine plume, and tip vortices [6].

Figure 10a contains the results for the pressure signature as the grid is refined. The X_N/L_{BODY} locations of interest are shown in the schematic in Figure 9 for reference to give insight into which areas of the geometry are impactful at the location of the pressure probe. The RANS solution is also included for reference as dashed lines, which is not dependent on the grid resolution. The relative difference in the pressure signature between the RANS and WMLES is computed as

$$\varepsilon_p = \frac{p_{WMLES} - p_{RANS}}{p_\infty}, \quad (9)$$

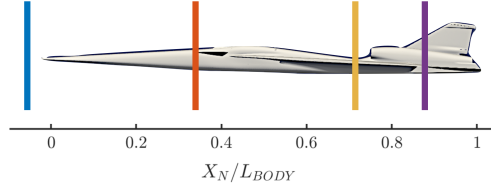
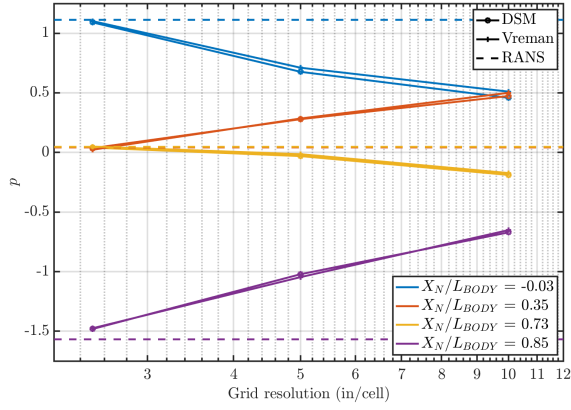
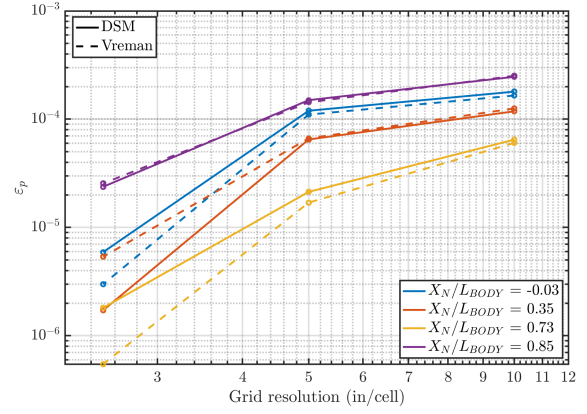


Fig. 9 Schematic of aircraft with delineations at specified locations.



(a) Pressure signature as a function of grid resolution.



(b) Relative pressure signature difference, ϵ_p , as a function of grid resolution.

Fig. 10 Pressure and ϵ_p for near-field pressure signature prediction.

where the subscripts denote either the WMLES or RANS solution. The results for ϵ_p , shown in Figure 10b, reveal that the difference between WMLES and RANS solution decreases with grid refinement for all locations considered and both SGS models.

C. Computational Cost

Cost-efficiency is part of the motivation for using WMLES for turbulence modeling. Table 3 outlines the calculations for the computational cost for different grid refinement configurations for the WMLES cases with the Vreman SGS model. This estimate is based on five flow passes through the domain to ensure convergence in the solution of the pressure signature propagated to one-body length below the aircraft. The number of characteristic steps in the simulation is determined using Δt estimated from the Courant number. The computational time in core-s is then converted to CPU-hr.

Table 3 Computational cost estimates for WMLES with Vreman SGS model.

	20 in/cell cone + 10 in/cell plane	10 in/cell cone + 5 in/cell plane	5 in/cell cone + 2.5 in/cell plane
CV (M)	3	18	135
Δt (s)	0.15	0.075	0.0375
Characteristic steps	25,000	50,000	100,000
Normalized time (core-s/CV/step)	12		
Total nodes	5		10
Total cores	240		480
CPU-hr	250	3000	45,000

Comparing the costs between WMLES and RANS simulations is not a straightforward task. In this regard, we refer to the cost reported by Spurlock et al. [48] as a reference. Spurlock et al. [48] performed RANS simulations for the AIAA Sonic Boom Prediction Workshop on the X-59 aircraft using the NASA Ames Electra cluster. Their setup involved one Skylake node equipped with two Intel Xeon Gold 6148 processors, utilizing a total of 40 cores for each run. The total computational time for their finest adapted grid, consisting of 29.6 million cells, was reported to be 1431 CPU-hours. As an example, the WMLES simulation using a grid configuration of 10 inches per cell for the cone and 5 inches per cell for the plane contains 18 million control volumes, which is comparable to the RANS simulation with 29.6 million control volumes. The estimated total computational time for WMLES using this specific solver is approximately 3000 CPU-hours. This indicates that, for a comparable grid resolution, WMLES is computationally more demanding than RANS but still exhibits a similar cost. It is important to note that improvements in computational cost can be achieved by optimizing the solver, utilizing faster CPUs, or employing GPUs, which can potentially lead to 7 to 10 times faster turnaround times. Nevertheless, our cost estimates highlight the motivation for future efforts in developing SGS models that offer higher accuracy for relatively coarser grids. Such advancements would directly result in reduced computational costs for WMLES solutions.

V. Conclusions

Current RANS methodologies have shown reasonable performance in predicting shock waves in regions far from their interactions with boundary layers. However, a practical RANS model capable of accurately addressing the broad range of flow regimes relevant to aerodynamic vehicles has yet to be developed. In recent years, WMLES has emerged as a tool for aerospace applications, offering a higher level of generality compared to RANS approaches. Nevertheless, the application of WMLES for predicting realistic supersonic aircraft has received less attention. In this work, we evaluated the performance of WMLES for realistic supersonic aircraft.

WMLES was utilized to analyze the experimental aircraft X-59 QueSST developed by Lockheed Martin at Skunk Works for NASA's Low-Boom Flight Demonstrator project. The simulations employed the charLES solver and aimed to assess the ability of WMLES to predict near-field noise levels under cruise conditions. The study considered two SGS models, the dynamic Smagorinsky model and the Vreman model, combined with an equilibrium wall model. The grid resolutions ranged from 20 in/cell to 5 in/cell in different areas of interest in the domain. The results were compared with previous numerical studies based on the RANS equations.

Our findings demonstrated that WMLES produced near-field pressure predictions that were similar to those of RANS simulations for the finest grid resolutions investigated at a comparable computational cost. This was the case for both SGS models. Some discrepancies were observed between the WMLES and RANS predictions downstream the aircraft. These differences persisted for the finest grid refinement considered, suggesting that they might be attributed to the intricate interactions of shock waves and expansion waves at the trailing edge. Note that the refinement for the finest grid resolution was limited to a rectangular region below the aircraft. As such, the interactions of shock waves and expansion waves outside the refined area might be still severely underresolved.

Here, our focus has been on WMLES with traditional SGS models along with comparisons with RANS predictions. Future simulations of the X-59 Low-Boom Flight Demonstrator will follow the wind tunnel experiments conducted NASA Glenn 8- by 6-Foot Supersonic Wind Tunnel [49, 50]. Our long-term objective is to develop a SGS model suitable for WMLES that offers accurate predictions across various flow regimes, encompassing both subsonic and supersonic flows. The findings obtained from the present study will guide the advancements needed to expand our current machine-learning based SGS modeling efforts [38–41] in the presence of shock waves.

Funding Sources

This material is based upon work supported by the U.S. Department of Energy, Office of Science, Office of Advanced Scientific Computing Research, Department of Energy Computational Science Graduate Fellowship under Award Number DE-SC0023112. This paper was prepared as an account of work sponsored by an agency of the United States Government. Neither the United States Government nor any agency thereof, nor any of their employees, makes any warranty, express or implied, or assumes any legal liability or responsibility for the accuracy, completeness, or usefulness

of any information, apparatus, product, or process disclosed, or represents that its use would not infringe privately owned rights. Reference herein to any specific commercial product, process, or service by trade name, trademark, manufacturer, or otherwise does not necessarily constitute or imply its endorsement, recommendation, or favoring by the United States Government or any agency thereof. The views and opinions of authors expressed herein do not necessarily state or reflect those of the United States Government or any agency thereof.

Acknowledgments

The authors acknowledge the MIT Supercloud and Lincoln Laboratory Supercomputing Center for providing HPC resources that have contributed to the research results reported within this paper.

References

- [1] Mani, M., and Dorgan, A. J., “A Perspective on the State of Aerospace Computational Fluid Dynamics Technology,” *Annual Review of Fluid Mechanics*, Vol. 55, No. 1, 2023, pp. 431–457. <https://doi.org/10.1146/annurev-fluid-120720-124800>.
- [2] Slotnick, J. P., Khodadoust, A., Alonso, J., Darmofal, D., Gropp, W., Lurie, E., and Mavriplis, D., *CFD Vision 2030 Study: A Path to Revolutionary Computational Aerosciences*, NASA CR-2014-218178, 2014.
- [3] Park, M. A., and Morgenstern, J. M., “Summary and Statistical Analysis of the First AIAA Sonic Boom Prediction Workshop,” *AIAA Journal of Aircraft*, Vol. 53, No. 2, 2016, pp. 578–598. <https://doi.org/10.2514/1.C033449>.
- [4] Park, M. A., and Nemec, M., “Near Field Summary and Statistical Analysis of the Second AIAA Sonic Boom Prediction Workshop,” *AIAA Journal of Aircraft*, Vol. 56, No. 3, 2019, pp. 851–875. <https://doi.org/10.2514/1.C034866>.
- [5] Carter, M. B., and Park, M. A., “Near Field Summary and Analysis of the Third AIAA Sonic Boom Prediction Workshop Shock-Plume Interaction Case,” *AIAA AVIATION 2020*, American Institute of Aeronautics and Astronautics, Reston, VA, 2020. (Submitted for publication).
- [6] Park, M. A., and Carter, M. B., “Low-Boom Demonstrator Near-Field Summary for the Third AIAA Sonic Boom Prediction Workshop,” *J. Aircr.*, Vol. 59, No. 3, 2022, pp. 563–577. <https://doi.org/10.2514/1.C036323>.
- [7] Casey, M., Wintergerste, T., European Research Community on Flow, T., and Combustion., *ERCOfTAC best practice guidelines: ERCOfTAC special interest group on “quality and trust in industrial CFD”*, ERCOfTAC, 2000.
- [8] Roy, C. J., and Blottner, F. G., “Review and assessment of turbulence models for hypersonic flows,” *Progress in Aerospace Sciences*, Vol. 42, No. 7, 2006, pp. 469–530. <https://doi.org/https://doi.org/10.1016/j.paerosci.2006.12.002>, URL <https://www.sciencedirect.com/science/article/pii/S0376042107000309>.
- [9] Spalart, P. R., Jou, W. H., Strelets, M., and Allmaras, S. R., “Comments on the feasibility of LES for wings, and on a hybrid RANS/LES approach,” *Advances in DNS/LES*, Greyden Press, Columbus, OH, Vol. 1, 1997, pp. 4–8.

- [10] Spalart, P. R., “Detached-eddy simulation,” *Annu. Rev. Fluid Mech.*, Vol. 41, 2009, pp. 181–202.
- [11] Kirz, J., “DLR TAU Near-Field Simulations for the Third AIAA Sonic Boom Prediction Workshop,” *J. Aircraft*, Vol. 59, No. 3, 2022, pp. 670–682. <https://doi.org/10.2514/1.C036397>.
- [12] Schwamborn, D., Gerhold, T., and Heinrich, R., “The DLR TAU-Code: Recent Applications in Research and Industry,” 2006.
- [13] Wada, Y., and Liou, M. S., “An Accurate and Robust Flux Splitting Scheme for Shock and Contact Discontinuities,” *SIAM Journal on Scientific Computing*, Vol. 18, No. 3, 1997, pp. 633–657. <https://doi.org/10.1137/S1064827595287626>.
- [14] Rumsey, C. L., “The NASA Juncture Flow Test as a Model for Effective CFD/Experimental Collaboration,” *2018 Applied Aerodynamics Conference*, 2018. <https://doi.org/10.2514/6.2018-3319>.
- [15] Lozano-Durán, A., Bose, S. T., and Moin, P., “Performance of Wall-Modeled LES with Boundary-Layer-Conforming Grids for External Aerodynamics,” *AIAA J.*, Vol. 60, No. 2, 2022, pp. 747–766. <https://doi.org/10.2514/1.J061041>.
- [16] Baldwin, B., and Lomax, H., “Thin-layer approximation and algebraic model for separated turbulentflows,” *16th aerospace sciences meeting*, 1978, p. 257.
- [17] Rumsey, C. L., “Compressibility considerations for kw turbulence models in hypersonic boundary-layer applications,” *J. Spacecr. Rockets*, Vol. 47, No. 1, 2010, pp. 11–20.
- [18] Gaitonde, D., and Shang, J., “Calculations on a double-fin turbulent interaction at high speed,” *11th Applied Aerodynamics Conference*, 1993, p. 3432.
- [19] Bose, S. T., and Park, G. I., “Wall-Modeled LES for Complex Turbulent Flows,” *Annu. Rev. Fluid Mech.*, Vol. 50, No. 1, 2018, pp. 535–561. <https://doi.org/10.1146/annurev-fluid-122316-045241>.
- [20] Choi, H., and Moin, P., “Grid-point requirements for large eddy simulation: Chapman’s estimates revisited,” *Phys. Fluids*, Vol. 24, No. 1, 2012, p. 011702.
- [21] Yang, X. I. A., and Griffin, K. P., “Grid-point and time-step requirements for direct numerical simulation and large-eddy simulation,” *Phys. Fluids*, Vol. 33, No. 1, 2021, p. 015108. <https://doi.org/10.1063/5.0036515>.
- [22] Bermejo-Moreno, I., Campo, L., Larsson, J., Bodart, J., Helmer, D., and Eaton, J. K., “Confinement Effects in Shock Wave/Turbulent Boundary Layer Interactions Through Wall-Modelled Large-Eddy Simulations,” *Journal of Fluid Mechanics*, Vol. 758, 2014, pp. 5–62. <https://doi.org/10.1017/jfm.2014.505>.
- [23] Zebiri, B., Piquet, A., Hadjadj, A., and Verma, S., “Shock-Induced Flow Separation in an Overexpanded Supersonic Planar Nozzle,” *AIAA Journal*, Vol. 58, No. 5, 2020, pp. 2122–2131. <https://doi.org/10.2514/1.J058705>.
- [24] Mettu, B. R., and Subbareddy, P. K., “Modeling Non-Equilibrium Effects in Wall Modeled LES of High-Speed Flows,” *AIAA Aviation 2019 Forum*, AIAA, 2019. <https://doi.org/10.2514/6.2019-3699>.

- [25] Bocquet, S., Sagaut, P., and Jouhaud, J., “A Compressible Wall Model for Large-Eddy Simulation with Application to Prediction of Aerothermal Quantities,” *Physics of Fluids*, Vol. 24, No. 6, 2012, p. 065103. <https://doi.org/10.1063/1.4729614>.
- [26] Iyer, P. S., and Malik, M. R., “Analysis of the Equilibrium Wall Model for High-Speed Turbulent Flows,” *Physical Review Fluids*, Vol. 4, No. 7, 2019. <https://doi.org/10.1103/PhysRevFluids.4.074604>.
- [27] Dawson, D. M., Lele, S. K., and Bodart, J., “Assessment of Wall-Modeled Large Eddy Simulation for Supersonic Compression Ramp Flows,” *49th AIAA/ASME/SAE/ASEE Joint Propulsion Conference*, AIAA, 2013.
- [28] Edwards, J. R., Choi, J.-I., and Boles, J. A., “Large Eddy/Reynolds-Averaged Navier-Stokes Simulation of a Mach 5 Compression-Corner Interaction,” *AIAA Journal*, Vol. 46, No. 4, 2008, pp. 977–991. <https://doi.org/10.2514/1.32240>.
- [29] Fang, J., Yao, Y., Zheltovodov, A., and Lu, L., *Large-Eddy Simulation of a Three-Dimensional Hypersonic Shock Wave Turbulent Boundary Layer Interaction of a Single-Fin*, 2015. <https://doi.org/10.2514/6.2015-1062>, URL <https://arc.aiaa.org/doi/abs/10.2514/6.2015-1062>.
- [30] Fu, L., Bose, S., and Moin, P., “Wall-Modeled LES of Three-Dimensional Intersecting Shock Wave Turbulent Boundary Layer Interactions,” , 2020.
- [31] Li, J., Grube, N. E., Priebe, S., and Martin, P., “Analysis of the large eddy simulation of a shock wave and turbulent boundary layer interaction,” *43rd AIAA Fluid Dynamics Conference*, 2013, p. 2734.
- [32] Helm, C. M., and Martín, M., “Large eddy simulation of two separated hypersonic shock/turbulent boundary layer interactions,” *Phys. Rev. Fluids*, Vol. 7, No. 7, 2022, p. 074601.
- [33] Yang, X., Urzay, J., Bose, S., and Moin, P., “Aerodynamic Heating in Wall-Modeled Large-Eddy Simulation of High-Speed Flows,” *AIAA Journal*, Vol. 56, No. 2, 2018, pp. 1–12. <https://doi.org/10.2514/1.J056240>.
- [34] Fu, L., Karp, M., Bose, S., Moin, P., and Urzay, J., “Equilibrium Wall-Modeled LES of Shock-Induced Aerodynamic Heating in Hypersonic Boundary Layers,” *Center for Turbulence Research Annual Research Briefs*, Vol. 2018, 2018, pp. 171–181.
- [35] Iyer, P. S., and Malik, M. R., “Wall-Modeled Large Eddy Simulation of Flow over a Wall-Mounted Hump,” *46th AIAA Fluid Dynamics Conference*, AIAA, 2016.
- [36] Iyer, P. S., and Malik, M. R., “Large-Eddy Simulation of Axisymmetric Compression Corner Flow,” *2018 Fluid Dynamics Conference*, AIAA, 2018.
- [37] Fukushima, Y., and Kawai, S., “Wall-Modeled Large-Eddy Simulation of Transonic Airfoil Buffet at High Reynolds Number,” *AIAA Journal*, Vol. 56, No. 6, 2018, pp. 2372–2388.
- [38] Lozano-Durán, A., and Bae, H. J., “Self-critical machine-learning wall-modeled LES for external aerodynamics,” *Center for Turbulence Research - Annual Research Briefs*, 2020, pp. 197–210.

- [39] Ling, Y., Arranz, G., Williams, E., Goc, K., Griffin, K., and Lozano-Duran, A., “Wall-modeled LES based on building-block flows,” *Center for Turbulence Research - Proceedings of the Summer Program*, 2022, pp. 5–14.
- [40] Arranz, G., Ling, Y., and Lozano-Durán, A., *Wall-modeled LES based on building-block flows: Application to the Gaussian Bump*, 2023. <https://doi.org/10.2514/6.2023-3984>, URL <https://arc.aiaa.org/doi/abs/10.2514/6.2023-3984>.
- [41] Lozano-Durán, A., and Bae, H. J., “Machine learning building-block-flow wall model for large-eddy simulation,” *Journal of Fluid Mechanics*, Vol. 963, 2023, p. A35. <https://doi.org/10.1017/jfm.2023.331>.
- [42] Moin, P., Squires, K., Cabot, W., and Lee, S., “A dynamic subgrid-scale model for compressible turbulence and scalar transport,” *Physics of Fluids*, Vol. 3, No. 11, 1991, pp. 2746–2757.
- [43] Lilly, D. K., “A proposed modification of the Germano subgrid-scale closure method,” *Phys. Fluids*, Vol. 4, No. 3, 1992, pp. 633–635. <https://doi.org/10.1063/1.858280>.
- [44] Vreman, A. W., “An eddy-viscosity subgrid-scale model for turbulent shear flow: Algebraic theory and applications,” *Phys. Fluids*, Vol. 16, No. 10, 2004, pp. 3670–3681. <https://doi.org/10.1063/1.1785131>.
- [45] Fu, L., Bose, S., and Moin, P., “Prediction of aerothermal characteristics of a generic hypersonic inlet flow,” *Theoretical and Computational Fluid Dynamics*, Vol. 36, No. 2, 2022, pp. 345–368.
- [46] Larsson, J., and Kawai, S., “Wall-modeling in large eddy simulation: length scales, grid resolution and accuracy,” *Phys. Fluids*, Vol. 24, 2012. <https://doi.org/10.1063/1.3678331>.
- [47] Reuther, A., Kepner, J., Byun, C., Samsi, S., Arcand, W., Bestor, D., Bergeron, B., Gadepally, V., Houle, M., Hubbell, M., Jones, M., Klein, A., Milechin, L., Mullen, J., Prout, A., Rosa, A., Yee, C., and Michaleas, P., “Interactive supercomputing on 40,000 cores for machine learning and data analysis,” *2018 IEEE High Performance Extreme Computing Conference (HPEC)*, IEEE, 2018, pp. 1–6.
- [48] Spurlock, W. M., Aftosmis, M. J., and Nemec, M., “Cartesian Mesh Simulations for the Third AIAA Sonic Boom Prediction Workshop,” *J. Aircr.*, Vol. 59, No. 3, 2022, pp. 708–724. <https://doi.org/10.2514/1.C036405>.
- [49] Durston, D. A., Wolter, J. D., Shea, P., Winski, C. S., Elmiligui, A. A., Carter, M. B., Langston, S., and Bozeman, M. D., *X-59 Sonic Boom Test Results from the NASA Glenn 8- by 6-Foot Supersonic Wind Tunnel*, 2023. <https://doi.org/10.2514/6.2023-4317>, URL <https://arc.aiaa.org/doi/abs/10.2514/6.2023-4317>.
- [50] Winski, C. S., Bozeman, M. D., Elmiligui, A. A., Flamm, J., Mears, L., Long, K., and Friedlander, D. J., *X-59 Air Data Probe Calibration Wind Tunnel Test*, 2023. <https://doi.org/10.2514/6.2023-4491>, URL <https://arc.aiaa.org/doi/abs/10.2514/6.2023-4491>.